Chinese Chemical Letters 35 (2024) 108923

Contents lists available at ScienceDirect

Chinese Chemical Letters

journal homepage: www.elsevier.com/locate/cclet

$Ti_3C_2T_x$ MXene wrapped, carbon-coated porous Si sheets for improved lithium storage performance

Hui Cheng[a], Yueming Liu[b], Zhongling Cheng[a], Xianying Wang[c,*], Na Huang[a], Haijiao Zhang[a,*]

[a] Institute of Nanochemistry and Nanobiology, School of Environmental and Chemical Engineering, Shanghai University, Shanghai 200444, China
[b] Shanghai Key Laboratory of Green Chemistry and Chemical Processes, School of Chemistry and Molecular Engineering, East China Normal University, Shanghai 200062, China
[c] Energy Materials Research Center AG Hydrogen Materials & Devices, CAS Key Laboratory of Materials for Energy Conversion, Shanghai Institute of Ceramics, Chinese Academy of Sciences (SICCAS), Shanghai 200050, China

ARTICLE INFO

Article history:
Received 5 July 2023
Revised 21 July 2023
Accepted 9 August 2023
Available online 12 August 2023

Keywords:
Si anodes
$Ti_3C_2Ti_x$ MXene
Porous structure
Interfacial assembly
Lithium-ion batteries

ABSTRACT

Si-based materials have shown great potential as lithium-ion batteries (LIBs) anodes due to their natural reserves and high theoretical capacity. However, the large volume changes during cycles and poor conductivity of Si lead to rapid capacity decay and poor cycling stability, ultimately limiting their commercial applications. Herein, we have skillfully utilized the microporous MCM-22 zeolite as the unique silicon source to produce porous Si (pSi) sheets by a simple magnesiothermic reduction, followed by a carbon coating and further $Ti_3C_2T_x$ MXene assembly, obtaining the ternary pSi@NC@TNSs composite. In the design, porous Si sheets provide more active sites and shorten Li-ion transport paths for electrochemical reactions. The N-doped carbon (NC) layer serves as a bonding layer to couple pSi and $Ti_3C_2T_x$. The conductive network formed by 2D $Ti_3C_2T_x$ and medium NC layer effectively enhances the overall charge transport of the electrode material, and helps to stabilize the electrode structure. Therefore, the as-made pSi@NC@TNSs anode delivers an improved lithium storage performance, exhibiting a high reversible capacity of 925 mAh/g at 0.5 A/g after 100 cycles. This present strategy provides an effective way towards high-performance Si-based anodes for LIBs.

Lithium-ion batteries (LIBs) as the primary battery technology need to consistently surpass the energy limit in order to better satisfy ever-growing demand for electric vehicles and smart grid, *etc*. In the development of LIBs anodes, Si has attracted widespread attention owing to its abundant sources, low electrochemical potential, and high theoretical specific capacity (≈3579 mAh/g for $Li_{3.75}Si$, 4200 mAh/g for $Li_{4.4}Si$) [1,2]. However, the enormous volume expansion generated during the process of lithiation/delithiation from Si anodes results in a series of problems such as electrode crushing, electrical isolation, and ultimately the rapid decay of capacity [3,4]. Additionally, the low conductivity and Li^+ diffusion coefficient of Si are also key issues, which greatly limit their commercial applications [5,6].

To address the above problems, various approaches have been proposed including decreasing the particle size, the engineering of the cavity, and the construction of composites [7]. Especially, porous Si (pSi) has been widely studied because of its high porosity, which can not only accommodate the large volume change and alleviate structural stress, but also promote the electrons/ions transport [8]. In addition, the carbon coating can also promote charge transfer and reduce the volume change of Si, and further improving the lithium storage capability [9]. Nevertheless, it is still challenging for the carbon interface to maintain long-term stability during deep cycles. So, there are still a strong demand to gain the high conductivity and structural stability of Si-based anodes [10,11]. In recent years, two-dimensional (2D) $Ti_3C_2T_x$ MXene has attracted more and more attention because of its good conductivity, rich surface chemical groups, and excellent Li^+ transport ability [12]. The electrochemical performance of Si anodes can be effectively improved by coupling with $Ti_3C_2T_x$ [13,14]. For instance, Zhang and co-workers assembled a sandwich structure of Si and MXene for LIBs anode, showing an excellent electrochemical property with a capacity of 643.8 mAh/g after 100 cycles at 0.3 A/g [15]. The above results indicate that $Ti_3C_2T_x$ MXene can compensate for the defects of Si anodes to some extent. Consequently, how

* Corresponding authors.
E-mail addresses: wangxianying@mail.sic.ac.cn (X. Wang), hjzhang128@shu.edu.cn (H. Zhang).

https://doi.org/10.1016/j.cclet.2023.108923
1001-8417/

to effectively cooperate pSi with the carbon coating and MXene to improve electrochemical performance is very meaningful.

In this work, porous Si is firstly prepared by a simple magnesiothermic reduction, subsequently encapsulated in the conductive network formed by the N-doped carbon (NC) layer and $Ti_3C_2T_x$ nanosheets (TNSs). The design of pSi can adapt the large volume changes during cycles. The NC layer provides a good conductivity and promotes the bonding between pSi and $Ti_3C_2T_x$. Meanwhile, TNSs can accelerate reaction kinetics and further enhance structural stability. When employed as the LIBs anode, the resulting pSi@NC@TNSs composite achieves an enhanced electrochemical performance.

The synthetic process of the ternary pSi@NC@TNSs composite is shown in Fig. 1a. Microporous MCM-22 zeolite (Fig. S1a in Supporting information) with layered structure is chosen as the Si precursor [16]. The microporous structure can provide a short channel for the rapid diffusion of magnesium vapor into the interior. Meanwhile, it promotes heat dispersion and minimizes the harm caused by the heat accumulation effect [17,18]. As shown in Fig. S1b (Supporting information), the as-prepared product has a uniform morphology similar to pristine MCM-22 after reduction. Differently, a large number of pores appear onto the surface of sheets, suggesting the formation of pSi. Next, the polydopamine-coated pSi (pSi@PDA) is prepared and further annealed at in Ar atmosphere, where the PDA layer is converted into the N-doped carbon layer, resulting in the formation of pSi@NC. It can be clearly seen from Fig. S2 (Supporting information), the thickness of carbon layer is about 10 nm. Then, pSi@PDA is modified by polymethyl methacrylate (PMMA) with positive charge, and TNSs is uniformly encapsulated onto the surface of PMMA-treated pSi@PDA *via* an electrostatic assembly [19]. Finally, the ternary pSi@NC@TNSs composite is successfully achieved after carbonization in inert atmosphere.

Fig. 1b shows the SEM image of the composite. Clearly, pSi@NC@TNSs exhibits a lamellar stacked structure with uniform morphology, and there are some crumpled nanosheets on its surface, suggesting the presence of $Ti_3C_2T_x$. TEM observations further confirm that the entire Si sheets are uniformly encapsulated by ultrathin TNSs (Fig. 1c). Moreover, the magnified TEM image (Fig. 1d) clearly reveals the appearance of a few layers of $Ti_3C_2T_x$ at the edge and internal porous structure of Si. The few-layer $Ti_3C_2T_x$ can provide more reversibly redox sites for Li^+, thereby enhancing the electrochemical properties [20,21]. Figs. 1e-g show the HRTEM images of pSi@NC@TNSs. In Fig. 1e, the lattice spacing of about 1.27 nm is ascribed to the (002) crystal plane of $Ti_3C_2T_x$ [22]. The lattice spacing of 0.31 nm is measured at the middle position in Fig. 1g, consisting with the (111) plane of crystal Si [23]. The (111), (220) and (311) planes of Si are shown in the SAED pattern (Fig. 1h). The results indicate that the MCM-22 zeolite has been successfully reduced to porous Si with high crystallinity. The EDS analysis of pSi@NC@TNSs (Fig. S3 in Supporting information) confirms the uniform distribution of $Ti_3C_2T_x$ and carbon on the pSi.

The principle of interface assembly is analyzed by FT-IR spectroscopy. As shown in Fig. S4 (Supporting information), the peak at 1486 cm^{-1} in pSi@PDA belongs to -NH_2, whereas the corresponding site absorption peak in the PMMA-modified pSi@PDA (pSi@PDA-PMMA) is clearly weakened and a distinct C–H bond absorption peak appears at 2950 cm^{-1} [24]. Furthermore, a new broad peak around 1660 cm^{-1} is caused by the amidation reaction between -NH_2 and -COOH, suggesting that PMMA has grafted onto the pSi@PDA [25]. And absorption peaks at 2950 cm^{-1} and 1660 cm^{-1} disappear in pSi@NC@TNSs, indicating that the PMMA has been removed after annealing [26]. Additionally, unmodified pSi@PDA cannot spontaneously assemble with TNSs under the same conditions (Fig. S5 in Supporting information), verifying the importance of grafting PMMA in the fabrication of pSi@NC@TNSs [24,27].

Fig. 2a presents the XRD patterns of different products. The sharp diffraction peaks at 28.4°, 47.2°, 55.9° and 69.2° correspond to the (111), (220), and (311) crystal faces of cubic Si (JCPDS No. 27–1402) [28]. The $Ti_3C_2T_x$ lamination peak at 7.9° is very weak in the XRD curve of pSi@NC@TNSs, because only a few layers of TNSs are formed in the composite [29,30]. Fig. 2b displays Raman spectra of pSi@NC@TNSs and pSi@NC with I_D/I_G values of 1.21 and 1.25, respectively, demonstrating the formation of amorphous carbon layer during heat treatment [31,32].

The porosity of the samples is then determined by N_2 sorption analysis. As shown in Fig. 2c, two samples both exhibit the distinct hysteresis at high pressure, indicating the existence of mesoporous structure. As evaluated by the pore size distribution curve (inset of Fig. 2c), there are two types of mesoporous, where the small pore size is centered at about 5 nm and the large pore size ranges from 20 nm to 40 nm. These abundant pores can provide

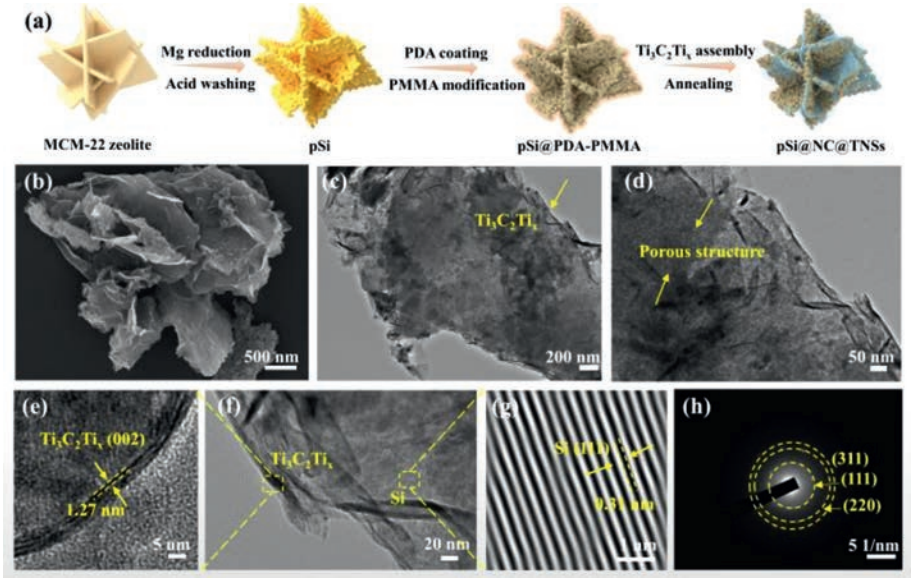

Fig. 1. (a) Schematic illustration of the typical preparation procedure of pSi@NC@TNSs. (b) SEM image, (c, d) TEM images, (e-g) HRTEM images, and (h) SAED pattern of pSi@NC@TNSs.

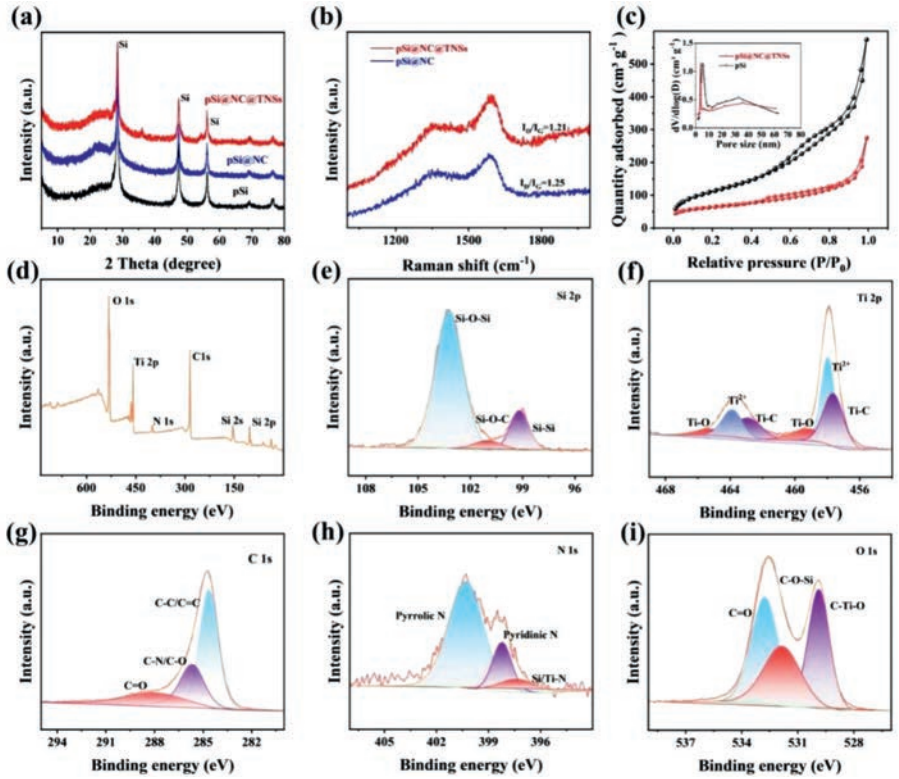

Fig. 2. (a) XRD patterns of pSi@NC@TNSs, pSi@NC and pSi. (b) Raman spectra of pSi@NC@TNSs and pSi@NC. (c) N_2 sorption isotherms and pore size distribution curves of pSi@NC@TNSs and pSi. (d) XPS survey scanning spectrum of pSi@NC@TNSs. High-resolution energy spectra of (e) Si 2p (f) Ti 2p (g) C 1s, (h) N 1s, (i) O 1s.

rapid transport channels for Li ions and accommodate large volume expansion during deep cycles. Additionally, pSi@NC@TNSs has a smaller BET surface area of 176.5 m^2/g than that of pSi (409.2 m^2/g), which is beneficial for reducing some side reactions during the discharging-charging processes.

The surface element valence states of pSi@NC@TNSs are characterized by XPS technique. As displayed in Fig. 2d, strong characteristic peaks of Si 2p, O 1s, Ti 2p, C 1s and N 1s appear in the survey spectra of pSi@NC@TNSs. In the Si 2p XPS spectrum (Fig. 2e), the peaks of 103.2, 101.1 and 99.2 eV are attributed to Si-O-Si, Si-O-C, Si-Si. The pSi and NC layer are covalently connected through Si-O-C bonds, providing a tight interface to promote the transport of Li^+ and structural stability [33,34]. The peaks at 459.2/465.1, 458.2/463.8 and 457.5/462.8 eV in the Ti 2p spectrum (Fig. 2f) are corresponding to Ti-O, Ti^{2+} and Ti-C bonds, respectively [35,36]. The C 1s spectrum (Fig. 2g) displays peaks of C=O, C–N, and C–C [37]. Fig. 2h shows the N 1s spectrum, the peaks at 397.4 eV, 398.2 eV and 400.2 eV are corresponding to Si/Ti-N, pyrrole nitrogen, pyridine nitrogen, respectively [38], which can provide more defects and enhance the chemical bond sum between Si and $Ti_3C_2T_x$ during heat treatment [39]. In the high-resolution O 1s spectrum (Fig 2i), the peaks center at 529.8, 531.8 and 532.7 eV belong to Ti-O-C, Si-O-C and C=O, respectively [40]. The results show that the covalent bond connects Si, N-doped carbon and $Ti_3C_2T_x$ to form a strong coupling interface.

To evaluate the electrochemical behavior of three samples as anodes for LIBs, cyclic voltammetry (CV) curves of pSi@NC@TNSs (Fig. 3a), pSi@NC (Fig. S6a in Supporting information) and pSi electrodes (Fig. S6c in Supporting information) are performed. A wide irreversible cathode peak at about 0.4–1.7 V for three samples, which is attributed to the formation of solid electrolyte interphase (SEI) film. In particular, the irreversible cathode peak area of pSi@NC@TNSs is minimal, implying a reduced loss of irreversible lithium and a superior structural stability [41]. The cathode peak at 0.01–0.3 V corresponds to the alloying of Si, and the anodic peak at about 0.36 and 0.53 V is related to the delithiation process of Li_xSi [42]. The CV curves of pSi@NC and pSi display similar anodic and cathodic peaks.

Fig. 3b displays the galvanostatic charge/discharge profiles of pSi@NC@TNSs at 0.2 A/g. The initial coulomb efficiency (ICE) of pSi@NC@TNSs is 65%, higher than those of pSi@NC (59%) and pSi (34%) (Figs. S6b and d in Supporting information). The gradually declining ICE is due to the large exposed surface area and the formation of thick SEI layer. The galvanostatic charge-discharge curves platform of three electrodes are consistent with their CV peaks and the polarization decreases with the increase of cycling, indicating a continuous activation process [43]. Fig. 3c shows the cycling performances of three electrodes. The reversible capacity is 925 mAh/g after 100 cycles of pSi@NC@TNSs at 0.5 A/g, which is much better than pSi@NC (688 mAh/g) and pSi (450 mAh/g). Furthermore, it also shows a good long-term cycling performance (Fig. S7 in Supporting information), maintaining a specific capacity of 726.3 mAh/g even after 500 cycles at 1 A/g. The TEM image (Fig. S8 in Supporting information) indicates that no serious cracking or pulverization can be seen after cycling, and the whole structure remains well, indicating an excellent structural stability of the pSi@NC@TNSs electrode. Their rate capabilities are presented in Fig. 3d. The specific capacities of pSi@NC@TNSs electrode are 1292.3, 1009.2, 750.8, 605.9 and 365.5 mAh/g at different current densities of 0.2, 0.5, 1, 2 and 5 A/g, respectively. When the current density is restored to 0.2 A/g, the capacity of pSi@NC@TNSs recovers to 1029 mAh/g with a capacity retention rate of 78%. Moreover, the pSi@NC@TNSs electrode exhibits much higher capacity retention rate than other two electrodes (Fig. 3e). Besides, the cycling properties of the pSi@NC@TNSs electrode are also compared with previously reported Si/MXene composites anodes (Fig. 3f and Table S1 in Supporting information), showing a significant advantage for lithium-ion storage. The enhanced reason in electrochemical per-

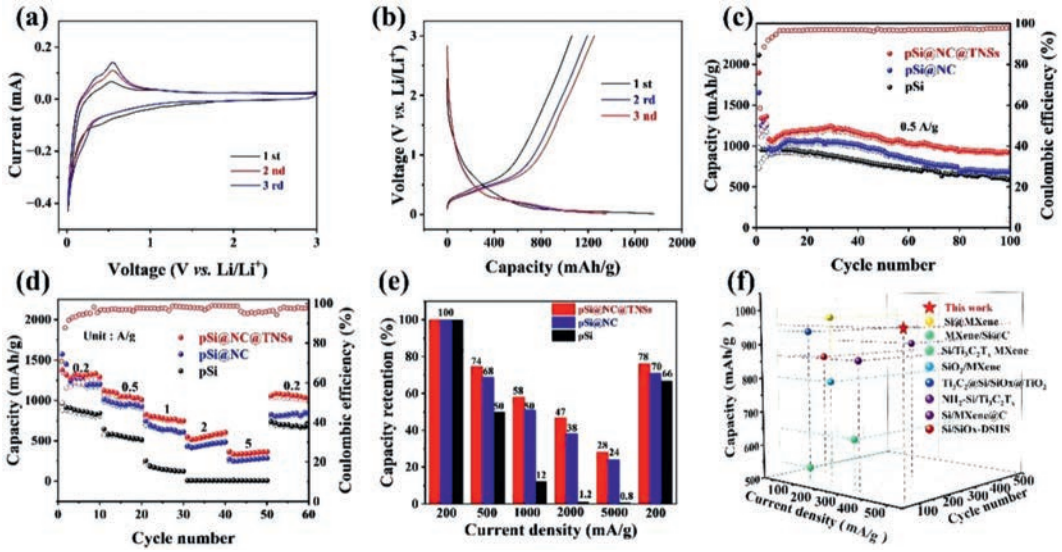

Fig. 3. (a) CV curves at a scan rate of 0.1 mV/s and (b) galvanostatic charge/discharge profiles of pSi@NC@TNSs at 0.2 A/g. (c) Cycling performances and coulombic efficiency at 0.5 A/g, (d) rate capabilities, and (e) capacity retention rates of pSi@NC@TNSs, pSi@NC and pSi electrodes. (f) Comparison of cycling performances between previously reported LIBs anode materials with this study. The details were listed in Table S1 (Supporting information).

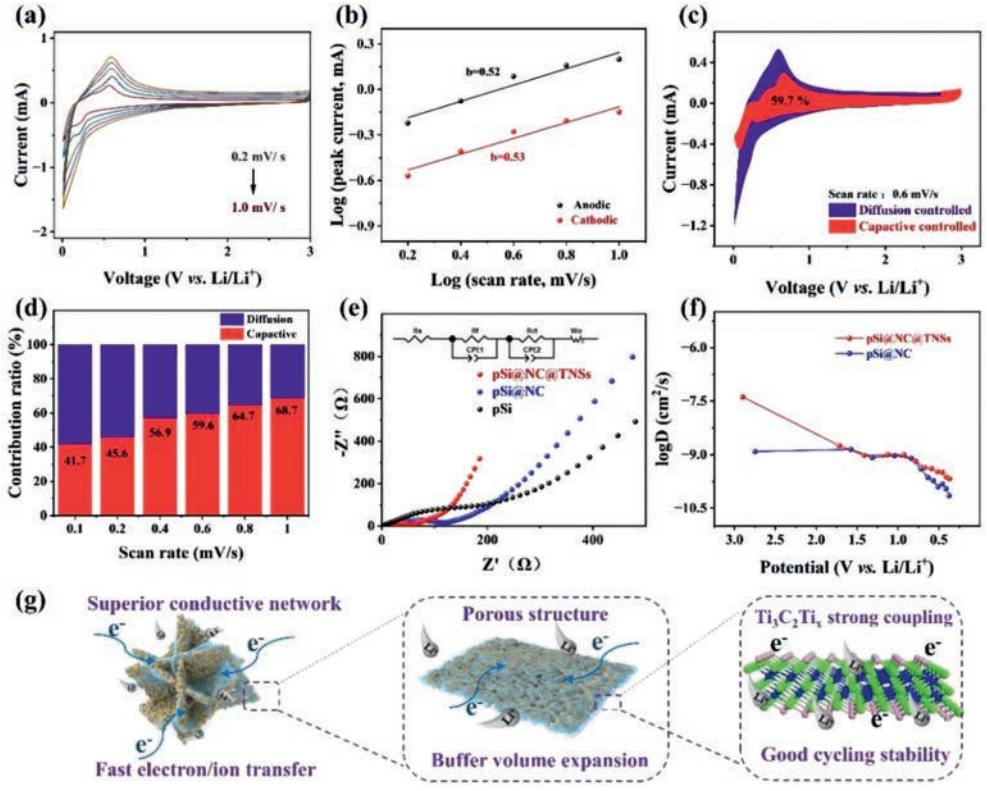

Fig. 4. (a) CV curves of the pSi@NC@TNSs electrode at different scan rates, (b) Plot of the relationship between log peak current and log scan rate, (c) Contributions of capacitance and diffusion control at 0.6 mV/s, (d) Percentage of capacitance and diffusion-controlled capacity at different scan rates. (e) Electrochemical impedance profiles and corresponding equivalent circuits of pSi@NC@TNSs, pSi@NC and pSi electrodes. (f) Li^+ chemical diffusion coefficients calculated from GITT results of pSi@NC@TNSs and pSi@NC electrodes. (g) Structural advantages of the pSi@NC@TNSs electrode for lithium-ion storage.

formance of pSi@NC@TNSs is mainly due to the synergistic effect among porous Si, N-doped carbon layer, and $Ti_3C_2T_x$ nanosheets.

The dynamical behavior of pSi@NC@TNSs is then analyzed by collecting a series of CV curves at different scan rates of 0.2–1.0 mV/s. As shown in Fig. 4a, all CV curves have similar shape at different scan rates, and peak currents increase with increase of scanning rates, indicating a fast storage of Li-ion and low polarization. The relationship between peak current (i) and scan rate (v) is as follows:

$$i = av^b \quad (1)$$

The b value can be used to examine the capacitance and diffusion control process of the electrode. As shown in Fig. 4b, the values of the cathode peak and anode peak are 0.74 and 0.67, respectively, which are close to 1, indicating a capacitive-dominated process for pSi@NC@TNSs. The contribution of capacitance and dif-

fusion control to capacity is analyzed by the following equations:

$$i(V) = k_1 v + k_2 v^{1/2} \quad (2)$$

In the equation, k_1 and k_2 are constants, and $k_1 v$, $k_2 v^{1/2}$ represent capacitive dominant effect and diffusion dominant effect [44]. The capacitance contribution rates gradually increase with the scan rates, and reach 78.1% at 0.6 mV/s (Figs. 4c and d), which are obviously higher than those of the pSi@NC (Fig. S9 in Supporting information), demonstrating that pSi@NC@TNSs can provide more active sites and further enhance the pseudo-capacitance energy storage.

Fig. 4e shows the Nyquist diagrams and the corresponding equivalent circuits of three electrodes. Obviously, the charge transfers impedance (R_{ct}) of pSi@NC@TNSs is significantly lower than pSi@NC and pSi electrodes, meaning a faster electron transfer. In addition, pSi@NC@TNSs electrode shows the lowest diffusion impedance (Z_w), indicating the rapid Li^+diffusion. The low resistance of pSi@NC@TNSs is assigned to well-constructed conductive backbone by $Ti_3C_2T_x$ and carbon and intimate interface contact, leading top referable reversible capacity and excellent cycling stability [43]. The Li-ion diffusion coefficients is calculated by the following formula:

$$D = \frac{4}{\pi \tau} \left(\frac{n_m V_m}{M_B S} \right)^2 \left(\frac{\Delta E_s}{\Delta E_\tau} \right)^2 \quad (3)$$

τ is the relaxation time and S is the contact area between electrode and electrolyte. n_m, M_B and V_m correspond to the molar mass, mass and volume of the electrode material, respectively, ΔE_S and ΔE_τ correspond to the voltage changes caused by pulse and constant current charging and discharging, respectively. Fig. 4f shows the calculated Li-ion diffusion coefficients of pSi@NC@TNSs and pSi@NC electrodes from galvanostatic intermittent titration technique (GITT) tests performed in the voltage range of 0.01–3.0 V, and the Li-ion diffusion coefficients of pSi@NC@TNSs is higher than that of pSi@NC, further indicating pSi@NC@TNSs has better Li-ion transport kinetics.

The structural advantages of the ternary pSi@NC@TNSs composite electrode for lithium-ion storage are briefly illustrated in Fig. 4g. In such a design, on one hand, the high surface area enables the Si active material and electrolyte full contact, and rich pore structure is more effective in alleviating the volume expansion during deep cycles. On the other hand, the superior conductivity and chemical flexibility of ultrathin $Ti_3C_2T_x$ nanosheets provide pseudo capacitance to contribute more storage capacity and a good protection for inner pSi. Meanwhile, the medium N-doped carbon layer serves as a bonding layer for strong coupling of pSi and $Ti_3C_2T_x$, as well as offers more defects for lithium storage. Therefore, the above synergistic effect in the pSi@NC@TNSs composite together contributes to the boosted electrochemical storage performance for LIBs.

In short, we develop a new ternary pSi@NC@TNSs composite with robust interface coupling *via* combining a simple magnesiothermic reduction with electrostatic assembly process. In the configuration, porous Si sheets derived from microporous MCM-22 zeolite effectively buffer the large volume changes, and the robust network constructed by $Ti_3C_2T_x$ and NC layer significantly enhances the conductivity and structural stability of the whole electrode material. In virtue of these benefits, the resulting pSi@NC@TNSs anode shows improved lithium-ion storage capability, delivering a high invertible discharge capacity of 925 mAh/g at 0.5 A/g and a good rate capability of 365.5 mAh/g at 5 A/g. The results provide an innovative idea for the preparation of porous Si materials and reasonable design of Si-based composites for advanced energy storage.

Declaration of competing interest

The authors declare that they have no known competing financial interests or personal relationships that could have appeared to influence the work reported in this paper.

Acknowledgments

The work was financially supported by the Natural Science Foundation of Shanghai (No. 23ZR1423800), Shuguang Program from Shanghai Education Development Foundation and Shanghai Municipal Education Commission (No. 18SG35), and Key Laboratory of Advanced Energy Materials Chemistry (Ministry of Education), Nankai University.

Supplementary materials

Supplementary material associated with this article can be found, in the online version, at doi:10.1016/j.cclet.2023.108923.

References

[1] S. Chae, S.H. Choi, N. Kim, et al., Angew. Chem. Int. Ed. 59 (2020) 110–135.
[2] Y. Cui, Nat. Energy 6 (2021) 995–996.
[3] G.J. Zhu, D.L. Chao, W.L. Xu, et al., ACS Nano 15 (2021) 15567–15593.
[4] Y. Chu, B. Xi, S. Xiong, Chin. Chem. Lett. 32 (2021) 1983–1987.
[5] C. Zhang, F. Wang, J. Han, et al., Small Structures 2 (2021) 2100009.
[6] P. Li, H. Kim, S.T. Myung, et al., Energy Storage Mater. 35 (2021) 550–576.
[7] J. Park, Y. Lee, H. Lee, et al., ACS Nano 14 (2020) 12–20.
[8] T. Song, H. Zhao, Y. Hu, et al., Chin. Chem. Lett. 30 (2019) 2347–2350.
[9] Q. Zhang, B. Xi, S. Xiong, et al., Inorg. Chem. Front. 8 (2021) 4282–4290.
[10] S. Kim, G. Yoon, S.K. Jung, et al., ACS Energy Lett. 8 (2022) 9–20.
[11] S. Zhou, C. Fang, X. Song, et al., Carbon Energy 2 (2020) 143–150.
[12] K. Guan, L. Dong, Y. Xing, et al., J. Energy Chem. 75 (2022) 330–339.
[13] X. Li, Z. Chen, A. Li, et al., ACS Appl. Mater. Interfaces 12 (2020) 48718–48728.
[14] X. Zhu, J. Shen, X. Chen, et al., Chem. Eng. J. 378 (2019) 122212.
[15] F. Zhang, Z.R. Jia, C. Wang, et al., Energy 195 (2020) 117047.
[16] R. Rojaee, R. Shahbazian-Yassar, ACS Nano 14 (2020) 2628–2658.
[17] N. Kim, H. Park, N. Yoon, et al., ACS Nano 12 (2018) 3853–3864.
[18] B.R. Wang, W.W. Li, T. Wu, et al., Energy Storage Mater. 15 (2018) 139–147.
[19] M.Q. Zhao, X. Xie, C.E. Ren, et al., Adv. Mater. 29 (2017) 1702410.
[20] C. Cui, R.Q. Dai, C. Zhang, et al., J. Mater. Chem. A 10 (2022) 15474–15484.
[21] P. Bärmann, M. Winter, J. Gonzalez-Julian, et al., Small 17 (2021) 2104130.
[22] X. Tian, P. Zhang, Y.Z. Liao, et al., Small Methods 2 (2023) e2201525.
[23] J. Zhou, Y. Lu, L.S. Yang, et al., Carbon Energy 4 (2022) 399–410.
[24] M.T. Xia, B.J. Chen, F. Gu, et al., ACS Nano 14 (2020) 5111–5120.
[25] X. Wan, T. Mu, B. Shen, et al., Nano Energy 99 (2022) 107334.
[26] Q. Li, Q.Z. Jiao, Y. Yan, et al., Chem. Eng. J. 450 (2022) 137922.
[27] X.L. Li, X.W. Yin, C.Q. Song, et al., Adv. Funct. Mater. 28 (2018) 1803938.
[28] Z.L. Cheng, H. Jiang, X.L. Zhang, et al., Adv. Funct. Mater. 3 (2023) 2301109.
[29] Y. Yan, X.L. Zhao, H.L. Dou, et al., ACS Appl. Mater. Interfaces 12 (2020) 18541–18550.
[30] L.Y. Xiu, Zhi Yu Wang, Meng Zhou Yu, et al., ACS Nano 12 (2018) 8017–8028.
[31] X. Sun, Y.Y. Wang, Y.M. Zhang, et al., Adv. Energy Sustain. Res. 3 (2022) 2200028.
[32] L.T. Tong, K.C. Long, L.B. Chen, et al., ACS Appl. Energy Mater. 5 (2022) 13877–13886.
[33] L. Liu, X.X. Li, G. He, et al., J. Alloys Compd. 836 (2020) 155407.
[34] P. Wu, X. Guo, Y. Zhong, et al., ACS Appl. Energy Mater. 5 (2022) 6373–6382.
[35] W.L. Wu, C.W. Wang, C.H. Zhao, et al., J. Colloid Interface Sci. 580 (2020) 601–613.
[36] F.Y. He, C. Tang, G.J. Zhu, et al., Sci. China Chem. 64 (2021) 964–973.
[37] Z.G. Liu, D.Z. Lu, W. Wang, et al., ACS Nano 16 (2022) 4642–4653.
[38] J. Wang, Z. Yang, B. Mao, et al., ACS Energy Lett. 7 (2022) 2781–2791.
[39] X. Han, W.J. Zhou, M.F. Chen, et al., J. Energy Chem. 67 (2022) 727–735.
[40] Z.H. Zhang, H.J. Ying, P.F. Huang, et al., Chem. Eng. J. 451 (2023) 138785.
[41] Y.J. Cai, T.H. Xu, N. von Solms, et al., Electrochim. Acta 340 (2020) 135990.
[42] X. Peng, C. Xiong, Y. Lin, et al., SmartMat 2 (2021) 579–590.
[43] P. Zhang, Q. Zhu, Z. Guan, et al., ChemSusChem 13 (2020) 1621–1628.
[44] Y. Chu, S. Xiong, Chin. Chem. Lett. 33 (2022) 486–490.